

Magnetic Control of Lateral Migration of Ellipsoidal Microparticles in Microscale Flows

Ran Zhou,¹ Christopher A. Sobecki,¹ Jie Zhang,¹ Yanzhi Zhang,² and Cheng Wang^{1,*}

¹*Department of Mechanical and Aerospace Engineering,
Missouri University of Science and Technology, Rolla, Missouri 65401, USA*

²*Department of Mathematics and Statistics, Missouri University of Science and Technology,
Rolla, Missouri 65401, USA*

(Received 10 November 2016; revised manuscript received 3 June 2017; published 21 August 2017)

Precise manipulations of nonspherical microparticles by shape have diverse applications in biology and biomedical engineering. Here, we study lateral migration of ellipsoidal paramagnetic microparticles in low-Reynolds-number flows under uniform magnetic fields. We show that magnetically induced torque alters the rotation dynamics of the particle and results in shape-dependent lateral migration. By adjusting the direction of the magnetic field, we demonstrate versatile control of the symmetric and asymmetric rotation of the particles, thereby controlling the direction of the particle's lateral migration. The particle rotations are experimentally measured, and their symmetry or asymmetry characteristics agree well with the prediction from a simple theory. The lateral migration mechanism is found to be valid for nonmagnetic particles suspended in a ferrofluid. Finally, we demonstrate shape-based sorting of microparticles by exploiting the proposed migration mechanism.

DOI: 10.1103/PhysRevApplied.8.024019

I. INTRODUCTION

In biology, shapes are an intrinsic biomarker of bioparticles [1], with examples including rodlike *E. coli*, disk-shaped red blood cells, and budding yeast cells. There is a critical need to manipulate nonspherical biological particles according to shapes in biomedical and biology applications because the shapes may be used as an indicator of the development stage or health status of the bioparticles. For instance, in researching eukaryotic-cell reproductions [2], yeast cells (commonly used model cells) need to be isolated based on their development stages, which can be identified by their shapes [3]. Malaria and sickle-cell anemia are accompanied with the changes of red blood cells from disk shapes to other shapes [4,5].

Traditional separation methods, such as size exclusion and mass- or density-based purification, are effective in separating microparticles by size. However, they are less effective for separating particles by shape [6]. Nonspherical microparticles, which are often suspended in fluid environments (e.g., biological fluids or culture media), are hard to separate by shape, for two reasons. First, nonspherical particles *rotate* in flows and present themselves with many possible sizes, rendering size-exclusion techniques (e.g., filtering) ineffective. Second, the sedimentation speed, due to centrifugal force, depends on both the particle orientation and the particle shape. Thus, even for particles of the same shape and size, the sedimentation speed may be different, making centrifugation less useful for separating nonspherical particles. More recently, microfluidic techniques—both passive and active methods—have demonstrated great potential as

the next-generation technology for separating cells and particles. However, a majority of the microfluidic techniques [7–9] are designed for microparticles having approximately spherical shapes. As a result, the capability of distinguishing shapes remains absent.

Recognizing the urgent need, a few studies have reported methods to achieve shape-based separation based on microfluidics. These efforts have included hydrodynamic filtering using branched channels [10] and obstacle arrays [11,12], inertia lift [13,14], dielectrophoresis (DEP) [15,16], viscoelastic fluids [17,18], and magnetophoresis in ferrofluids [19]. Although effective (to some extent), these methods have their limitations. The hydrodynamic approaches require sophisticated designs of highly complex branched channels [10] and high-resolution arrays comparable to the smallest dimension of particle size [12]. The inertia-based techniques [20] operate at high flow rates, which can be a challenge when samples are precious and available only in small quantities. DEP requires the integration of active electrode elements, and a precise and reproducible control of the buffer conductivity between each experiment [15,16]. The use of viscoelastic fluids requires a subtle and sensitive balance between elastic lift and inertia forces [17,18]. The negative-magnetophoresis method reported by Zhou and Xuan [19] relies on a nonuniform magnetic field, as well as on shape-dependent magnetic and drag forces, both of which are difficult to predict analytically. In addition, the magnetic forces require a well-controlled magnetic field gradient, which is challenging to implement for microscale devices.

In this work, we demonstrate an alternative shape-dependent migration mechanism of rigid ellipsoidal microparticles in combined magnetic and flow fields. It is shown that in the regime of weak magnetic strength, the symmetry

*wancheng@mst.edu

property of the particle rotation is modified due to the magnetically induced torque, and it depends on the direction of the applied magnetic field. This finding can also be in good analogy with deformable particles, such as red blood cells (RBCs). For example, RBC deformability results in an averaged asymmetric shape and leads to a nonzero lift and migration law similar to the one known for a fixed shape and orientation [21]. Therefore, the mechanism in this paper could be extended to soft or deformable bioparticles, though deformable particles are expected to have much more complex motion in shear flows [22–25]. In our study, coupled with hydrodynamic interactions with the wall, the magnetic field can result in directional control of the lateral migration of the ellipsoidal particles: (1) lateral migration toward, (2) away from the channel center, or (3) negligible lateral migration. In the regime with a stronger magnetic effect, the particles assume a quasi-steady-state angle. Using high-speed imaging, we experimentally quantify the rotation dynamics of single particles, which is in good agreement with the prediction of a simple theory.

We further demonstrate particle separation by shape by using the shape-dependent migration mechanism. Such a separation method is different from existing methods that are based on magnetic forces [26–28], which are largely dependent on particle size or volume, but not on shape. Because of the uniform magnetic field [29], in our method, there is no magnetic force acting on the particles. Rather, the shape-dependent magnetic torque controls the particle rotation and induces shape-dependent separation. The approach demonstrated here is applicable to both magnetic and nonmagnetic microparticles, including bioparticle complexes resulting from a binding of nanomagnetic particles to cells, and naturally existing diamagnetic (nonmagnetic) bioparticles. Particularly, shape-based manipulations can be realized by suspending these nonmagnetic bioparticles in ferrofluids [30–32], thanks to recent progress in biocompatible ferrofluids [33,34].

II. EXPERIMENTAL SETUP

In our experiments, as depicted in Fig. 1(a), a microfluidic device is placed in the center of a uniform magnetic field of strength $H_0 \approx 35\,000$ A/m, which is generated by a Halbach array [35]. The microfluidic device is fabricated in polydimethylsiloxane following a previously reported soft lithography technique [36]. The width, the depth, and the

total length of the microfluidic channel are $w_c = 50\ \mu\text{m}$, $d_c = 35\ \mu\text{m}$, and $L = 20\,000\ \mu\text{m}$, respectively, as shown in Fig. 1(b). The microfluidic device consists of two inlets in Figs. 2(a)–2(d) or three inlets in Figs. 2(e)–2(h), and one outlet for all of the channels. The sample ellipsoidal particles used in this work are magnetite-doped and uncross-linked polystyrene microparticles. They are prepared from the original spherical paramagnetic particles by using the film-stretching approach of Ho *et al.* [37]. The aspect ratio of the ellipsoidal particles is $r_p = 4 \pm 0.4$, as measured from microphotographs. The mean diameter of the spherical paramagnetic particles is $d = 7\ \mu\text{m}$ (coefficient with a variation $< 5\%$, Micromod GmbH, Germany), its density is $\rho_p = 1100\ \text{kg/m}^3$, and its magnetic susceptibility is $\chi_p \approx 0.26$ [38].

Figure 2 demonstrates the particle migration without a magnetic field ($H_0 = 0$) and with a magnetic field of strength $H_0 \approx 35\,000$ A/m oriented at three different directions (indicated by the angle α). Two or three syringe pumps (NE-300, New Era and KDS 200, KDS Scientific) are used to control the flow rate of each inlet. In Figs. 2(a1)–2(d1), inlet 1 is injected with a 40-wt % aqueous-glycerol solution at a flow rate $Q_1 = 1.0\ \mu\text{l/min}$ to work as buffer flow, while inlet 2 is injected with a 40-wt % aqueous-glycerol solution containing sample particles at a flow rate $Q_2 = 0.2\ \mu\text{l/min}$. The particles are centered in the midplane (in the z direction) because the external magnetic field’s central plane is aligned with the midplane (in the z direction) of the flow field. The 40-wt % glycerol solution and the sample particles are density matched to prevent particle sedimentation. The aqueous-glycerol solution has a density $\rho_f \approx 1.1 \times 10^3\ \text{kg/m}^3$ and a viscosity $\eta_f \approx 0.0037\ \text{kg/(m s)}$. Similarly, in Figs. 2(e1)–2(h1), inlets 1 and 3 are injected with glycerol solutions at flow rates of $Q_1 = Q_3 = 0.5\ \mu\text{l/min}$, while inlet 2 is injected with a glycerol solution with particles at a flow rate $Q_2 = 0.2\ \mu\text{l/min}$. The Reynolds numbers are small for typical experimental conditions: flow Reynolds number $\text{Re} = [(\rho_f U D_h)/\eta_f] \sim 0.1$, where D_h is the hydraulic diameter of the channel, and particle Reynolds number $\text{Re}_p = (d_p/D_h)^2 \text{Re} \sim 0.01$, where d_p is the equivalent spherical diameter of the particle. Note that the definition of Re_p , which was introduced by Ho and Leal [39], accounts for the moving velocity of the particles and is different from the one often used for a stationary particle.

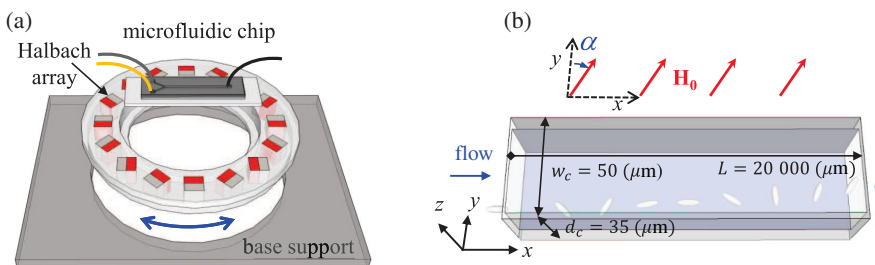


FIG. 1. (a) Schematic illustration of the microdevice located in a uniform magnetic field generated by a Halbach array. (b) 3D schematic of the microfluidic channel.

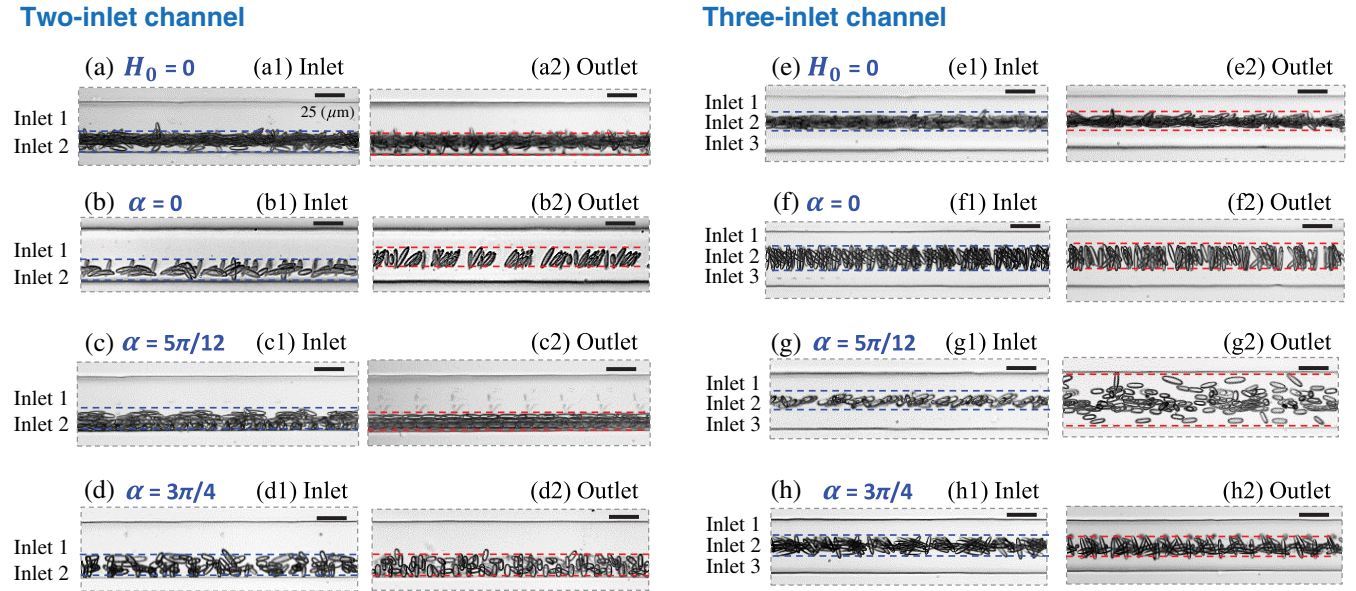


FIG. 2. Overview of the particle migration. (a)–(d) Particle distributions at the inlet and the outlet when they are injected from the bottom part of the channel under the condition (a) without an external magnetic field or (b)–(d) with the orientation of a magnetic field is $\alpha = 0$, $\alpha = 5\pi/12$, and $\alpha = 3\pi/4$. (e)–(h) Particle distributions at the inlet and the outlet when they are injected from the central part of the channel under a similar condition as (a)–(d). The total flow rates are $Q_t = 1.2 \mu\text{l}/\text{min}$ for each group, and $H_0 \approx 35\,000 \text{ A/m}$ in (b)–(d) and (f)–(h).

To record the trajectories of the paramagnetic particles during the experimental process, the microfluidic devices are mounted on an inverted microscope stage (IX73, Olympus). A high-speed camera (Phantom Miro M310, Vision Research) is used to capture high-speed videos up to 10 000 frames/s. IMAGEJ [40] and custom MATLAB codes are used to extract and analyze the orientation and position information of the particles from the experimental videos.

As can be seen in Fig. 2, when $\alpha = 0$ and $\alpha = 5\pi/12$, the ellipsoids migrate toward and away from the channel center, respectively. When $H_0 = 0$ or $\alpha = 3\pi/4$, particles exhibit no observable lateral migration between the inlet and the outlet. The directional migration of the particle under the influence of the magnetic field are rather interesting because these particles experience zero magnetic force in a uniform magnetic field [29], no matter in which direction the magnetic field is imposed. How does it happen? In the rest of this paper, we focus on understanding this alternative particle-migration mechanism.

III. THEORETICAL ANALYSIS

In this section, we present a simple theoretical analysis on particle rotation in a simple shear flow bounded by a solid wall in the presence of a uniform magnetic field. Note that the model is different from the actual experiments. Moreover, the particle dynamics in bounded flows—not to mention the nonspherical shape, the confinement effect, and the nonlinear velocity profiles—is inherently complex. Thus, a quantitative prediction of the migration velocity would require full 3D numerical modeling. However, the

purpose of the model presented herein is to provide a qualitative understanding of the effect of the magnetic field (its magnitude and direction) on the observed lateral migration of the particles.

A. Ellipsoidal particles in shear flows

Consider a prolate ellipsoidal particle (with semimajor axis a and semiminor axes $b = c$) that is transported by a simple shear flow $u = \dot{\gamma}y$, with $\dot{\gamma}$ denoting the shear rate, as shown in Fig. 3(a). A particle that lies in the x - y plane

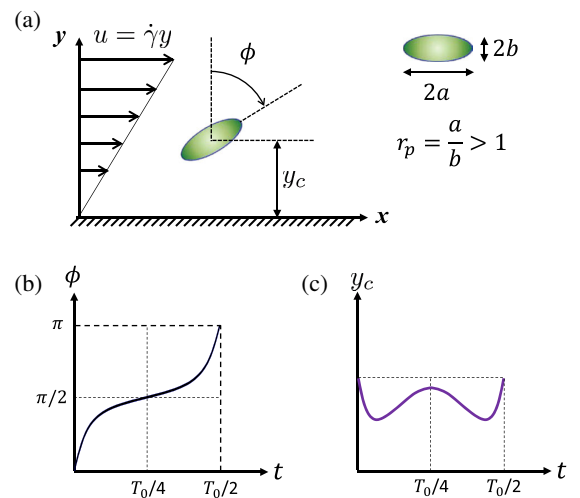


FIG. 3. (a) Illustration of a prolate ellipsoidal particle in a wall-bounded shear flow. (b) Evolution of angle ϕ vs time. (c) Oscillatory motion of the particle centroid in the y direction, y_c , over a π period.

rotates periodically. It is assumed that both fluid and particle inertia are negligible, based on typical experimental conditions. The particle rotation can be approximately described by Jeffreys's theory [41–43], even though the theory has been developed for particles in an unbounded flow. As shown in Fig. 3(b), the angular velocity of the particle is [44]

$$\omega_h = \frac{d\phi}{dt} = \dot{\gamma} \frac{(r_p^2 \cos^2 \phi + \sin^2 \phi)}{r_p^2 + 1}, \quad (1)$$

where ϕ is the angle measured from the velocity-gradient direction, and $r_p = a/b$ is the particle aspect ratio. The period over a rotation of 2π in an unbounded flow is $T_0 = 2\pi(r_p + r_p^{-1})/\dot{\gamma}$. A correction factor may be used to account for the increasing resistance due to the wall effect [43].

Different from unbounded flows, the presence of the wall induces a nonzero lift velocity perpendicular on nonspherical particles to the wall [42,45]. This lift velocity is due to a vertical force arising from the coupling of the rotational and translational motion and their hydrodynamic interactions with the wall. Numerical calculations show that the lift force is an antisymmetric function of ϕ with respect to $\phi = \pi/2$ [42]. As a result, the particle centroid oscillates away and toward the wall over a rotation cycle of π [41,45–49], as illustrated in Fig. 3(c). The amplitude of the oscillatory motion depends on the particle-wall separation distance, shear rate, and particle shape. In the absence of external force fields and particle inertia, the nonspherical particles have a zero net lateral migration during one period of rotation [41,42,47].

B. Ellipsoidal particles in combined flow and magnetic fields

When subject to an externally applied magnetic field, the particle will experience a torque, provided that the particle and the surrounding fluid have different magnetic susceptibilities [29]. In a uniform magnetic field \mathbf{H}_0 , the magnetic torque is $\mathbf{T}_m = \mu_0 \int_{V_p} [(\mathbf{M}_p - \mathbf{M}_f) \times \mathbf{H}_0] dV$, where $\mu_0 = 4\pi \times 10^{-7} \text{N/A}^2$ is the magnetic permeability of the vacuum, \mathbf{M}_p and \mathbf{M}_f are the magnetization of the particle and

the fluid, and V_p is the volume of the particle. Assuming that the particle and the fluid are homogeneous, isotropic, and linearly magnetizable, the magnetic torque due to the uniform magnetic field is $\mathbf{T}_m = \mu_0 V_p (\chi_p - \chi_f) \mathbf{H}^- \times \mathbf{H}_0$, where \mathbf{H}^- is the magnetic field inside the particle and χ_p and χ_f are the magnetic susceptibilities of the particle and the fluid, respectively [29,50].

In the experiments, the applied magnetic field \mathbf{H}_0 is parallel to the x - y plane and is directed at an angle α to the positive y axis [in Fig. 1(b)]. Thus, we restrict our analysis to particles lying in the x - y plane. It can be shown that the magnetic torque in the x - y plane (i.e., about the z axis) is

$$T_{mz} = -\frac{1}{2} V_p \times \frac{\mu_0 (\chi_p - \chi_f)^2 H_0^2 (D_{yy} - D_{xx}) \sin(2\phi - 2\alpha)}{[1 + \chi_f + (\chi_p - \chi_f) D_{xx}] [1 + \chi_f + (\chi_p - \chi_f) D_{yy}]}, \quad (2)$$

where H_0 denotes the magnitude of the applied magnetic field, D_{xx} and D_{yy} are the diagonal components of the ellipsoidal demagnetizing factor \mathbf{D} , and $D_{xx} = 1 - A$, $D_{yy} = A/2$, with A denoting the elliptical integral. For a prolate ellipsoid, $A = [r_p^2 / (r_p^2 - 1)] - [r_p \cosh^{-1} r_p / (r_p^2 - 1)^{3/2}]$ [51]. In Eq. (2), D_{xx} and D_{yy} are both less than 1. The magnetic susceptibility χ is positive for paramagnetic or ferromagnetic materials, and only marginally smaller than zero ($\leq -10^{-3}$) for diamagnetic materials. It is clear that the magnetic torque will have the same sign due to the dependence on $(\chi_p - \chi_f)^2$, for both diamagnetic particles in a ferrofluid or paramagnetic particles in a diamagnetic fluid.

With negligible particle inertia and wall effect, the angular velocity ω_m , due to the magnetic torque, is [52]

$$\omega_m = -\left(\frac{\mu_0 H_0^2}{\eta}\right) (\chi_p - \chi_f)^2 \sin(2\phi - 2\alpha) \lambda(r_p, \chi_p, \chi_f), \quad (3)$$

where η is the dynamic viscosity of the suspending fluid, and

$$\lambda(r_p, \chi_p, \chi_f) = \frac{(r_p^2 D_{xx} + D_{yy})(D_{yy} - D_{xx})}{4(r_p^2 + 1)[(1 + \chi_f) + (\chi_p - \chi_f) D_{xx}][(1 + \chi_f) + (\chi_p - \chi_f) D_{yy}]}. \quad (4)$$

The particle rotation due to the hydrodynamic and magnetic effects is additive [53], and thus the total angular velocity is $\omega_c = \omega_h + \omega_m$. We observe that ω_h varies from $\dot{\gamma}/(r_p^2 + 1)$ to $r_p^2 \dot{\gamma}/(r_p^2 + 1)$, while ω_m varies from $-\{[\mu_0 H_0^2 (\chi_p - \chi_f)^2]/\eta\} \lambda(r_p, \chi_p, \chi_f)$ to $\{[\mu_0 H_0^2 (\chi_p - \chi_f)^2]/\eta\} \lambda(r_p, \chi_p, \chi_f)$. A dimensionless parameter S is thus defined to measure the relative strength between the magnetic and flow fields,

$$S = \frac{\mu_0 (\chi_p - \chi_f)^2 H_0^2}{\eta \dot{\gamma}} (r_p^2 + 1) \lambda(r_p, \chi_p, \chi_f). \quad (5)$$

The magnetic torque tends to align the major axis of the particle to the direction of the magnetic field. As a result, ω_h and ω_m may oppose or assist each other for different ranges of ϕ during the rotation. When the magnetic field is

sufficiently strong, it can completely *impede* the rotation of the particle. In other words, the particle stops rotating if there exists a physically meaningful solution to $\omega_c = \omega_h + \omega_m = 0$. Denoted as S_{cr} , the critical value of S for the existence of real solutions to $\omega_c = 0$ can be found to be

$$S_{\text{cr}} = \frac{1}{2} \left[\sqrt{(r_p^2 - 1)^2 \sin^2(2\alpha) + 4r_p^2} - (r_p^2 - 1) \sin(2\alpha) \right]. \quad (6)$$

When $S < S_{\text{cr}}$, the particle executes complete rotations. Let T_c represent the period of rotation for ϕ from 0 to π . Then we can find that, by numerical integration,

$$T_c = \int_0^\pi \frac{d\phi}{\omega_c} = \frac{(r_p^2 + 1)}{\dot{\gamma}} \times \int_0^\pi \frac{d\phi}{(r_p^2 \cos^2 \phi + \sin^2 \phi) - S \sin(2\phi - 2\alpha)}. \quad (7)$$

The time taken from ϕ from 0 to 2π will be $2T_c$ because of the fore-aft symmetry of the ellipsoidal particles. The magnetic torque not only influences the angular velocity and rotational period but also breaks the symmetry property of the particle rotation. In an earlier study, asymmetric particle rotation was reported for an electric field perpendicular to the flow direction [53]. Under this electric field, the particle spent a longer time for the rotation from $\phi = 0$ to $\pi/2$ than that from $\pi/2$ to π [53]. In this study, the direction of the magnetic field, characterized by the angle α , is arbitrary; thus, its effect on the particle rotation needs to be understood. Let T'_c be the time taken for the particle to rotate from $\phi = 0$ to $\phi = \pi/2$, i.e.,

$$T'_c = \frac{(r_p^2 + 1)}{\dot{\gamma}} \int_0^{\pi/2} \frac{d\phi}{(r_p^2 \cos^2 \phi + \sin^2 \phi) - S \sin(2\phi - 2\alpha)}. \quad (8)$$

To characterize the symmetry or asymmetry of the particle rotation, we introduce a ratio parameter τ as

$$\tau = \frac{T'_c}{T_c}, \quad (9)$$

which can be calculated from Eqs. (7) and (8).

For a given $S < S_{\text{cr}}$, of particular interest is the effect of the direction of the magnetic field on τ , i.e., the dependence of τ on α . As shown in Fig. 4, we observe that (a) $\tau > 0.5$ when $0 < \alpha < \pi/4$ or $3\pi/4 < \alpha < \pi$, (b) $\tau < 0.5$ when $\pi/4 < \alpha < 3\pi/4$, and (c) $\tau = 0.5$ when $\alpha = \pi/4$ or $\alpha = 3\pi/4$. Moreover, τ grows farther away from 0.5 as S increases, meaning that the asymmetry of the rotation is more prominent because a larger S represents a stronger magnetic effect relative to the hydrodynamic effect.

When $S > S_{\text{cr}}$, the particle cannot execute complete rotations. The particle will then assume a steady (or

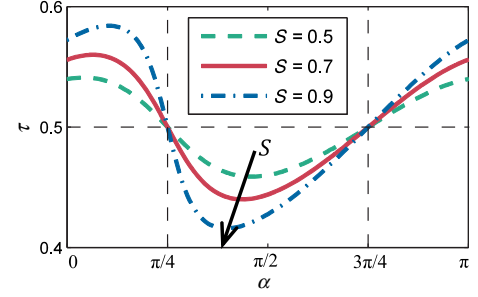


FIG. 4. Relationship curve between τ and magnetic-field orientation α .

quasisteady) orientation at $\phi = \phi^s$. The steady angle ϕ^s can be determined by solving $\omega_c = 0$, which gives two solutions,

$$\phi_{\pm}^s = \arctan \left(\frac{S \cos(2\alpha) \pm Q_\alpha}{[1 - S \sin(2\alpha)]} \right), \quad (10)$$

where $Q_\alpha = \sqrt{S^2 + S \sin(2\alpha)(r_p^2 - 1) - r_p^2}$. The stability of the two solutions can be determined by evaluating $d\omega_c/d\phi$ at ϕ_{\pm}^s . By numerical computation, it is found that $[(d\omega_c)/d\phi]|_{\phi_{\pm}^s}$ is always negative; thus, $\phi_{+}^s = \arctan \{ [S \cos(2\alpha) + Q_\alpha] / [1 - S \sin(2\alpha)] \}$ is the stable steady angle. The other solution, $\phi_{-}^s = \arctan \{ [S \cos(2\alpha) - Q_\alpha] / [1 - S \sin(2\alpha)] \}$, is unstable due to $[(d\omega_c)/d\phi]|_{\phi_{-}^s} > 0$ (see Appendix A).

C. Implications of symmetry of particle rotation on lateral migration

In the *absence* of magnetic fields, the particles rotate periodically and spend equal amounts of time for $0 < \phi < \pi/2$ and $\pi/2 < \phi < \pi$, i.e., $\tau = 0.5$. Owing to the nonspherical shapes of the particles and the hydrodynamic interactions with the wall [42], the particles experience an orientation-dependent lift force along the y direction, $F_L(\phi)$. The particle centroids oscillate in the y direction but have a zero migration over one complete period [45,46,48,49] because of the symmetric rotation of the particle.

In the *presence* of magnetic fields and with $S < S_{\text{cr}}$, the particle rotation now has three possible regimes: $\tau > 0.5$, $\tau < 0.5$, or $\tau = 0.5$. Owing to a change of the symmetry property of the particle rotation, we expect that the broken symmetry can cause a change of the net lateral migration of the particles. We hypothesize that the rotation asymmetry will result in one of three outcomes: (i) a net lift force toward the channel center (the region of lower shear) when $\tau > 0.5$, (ii) a net lift force toward the channel wall (the region of higher shear) when $\tau < 0.5$, or (iii) a zero net lift force when $\tau = 0.5$. However, because of the complex particle-wall hydrodynamic interaction, the nonspherical particle shape, and the finite size of the particle, it is

difficult to obtain analytical solutions of the lateral migration velocity even in simple flow configurations [42].

Here, we use numerical simulations to assess the effect of τ on the lateral migration of the particle. Assuming negligible fluid and particle inertia, we decompose the particle-fluid problem by linear superposition into four steady-state problems: (a) a simple shear flow $u_f = \dot{\gamma}y$ over a stationary particle, (b) a particle rotating at ω_p in a quiescent fluid, (c) a particle translating at u_p in the x direction in a quiescent fluid, and (d) a particle translating to v_p in the y direction in a quiescent fluid. In the simulations, the particle is held fixed at (x_0, y_0, z_0) , while the orientation of the particle ϕ is allowed to change from 0 to π . Owing to negligible particle inertia, the particle motion is quasisteady; thus, the total force and torque are both zero, allowing us to find the particle velocities u_p and v_p to satisfy the force-free and torque-free conditions. Similar approaches have been used in previous studies to find the lift force on spherical [20] and nonspherical particles [42]. Note that v_p would be the lateral migration velocity if the particle were allowed to move in the y direction. By choosing a set of parameters ($S, r_p, \dot{\gamma}, x_0, y_0, z_0$) and varying α , our numerical simulations show that (i) $\int_0^{T_c} v_p dt > 0$ when $\tau > 0.5$, (ii) $\int_0^{T_c} v_p dt < 0$ when $\tau < 0.5$, and (iii) $\int_0^{T_c} v_p dt \approx 0$ when $\tau = 0.5$ (see Appendix B).

IV. RESULTS AND DISCUSSION

A. Rotation and lateral migration of particles

Figures 5(a1)–5(a4) are the stacked images obtained from a series of high-speed videos taken at 10 000 frames/s, and they show particle rotations over a complete π period under different experimental conditions. These conditions include $H_0 = 0$ [Fig. 5(a1)], $H_0 \approx 35\,000$ A/m and $\alpha = 0$ [Fig. 5(a2)], $H_0 \approx 35\,000$ A/m and $\alpha = 5\pi/12$ [Fig. 5(a3)], and $H_0 \approx 35\,000$ A/m and $\alpha = 3\pi/4$ [Fig. 5(a4)]. The experimentally measured $\phi(\tilde{t})$ values within a π period are summarized in Figs. 5(b1)–5(b4). To compare the difference of the particle rotations, the dimensionless time $\tilde{t} = t/T_c$ is used here. We also measure the y position of the particle centroid over a period of rotation and estimate the vertical velocities, as shown in Figs. 5(c1)–5(c4).

When $H_0 = 0$, the particle rotation compares well with the prediction of the Jeffreys theory, as can be seen in Fig. 5(b1). The particle spends about an equal amount of time from $\phi = 0$ to $\phi = \pi/2$, and $\phi = \pi/2$ to $\phi = \pi$, i.e., $t_1 = t_2$. The particle centroid shows oscillatory motion in the y direction [Fig. 5(c1)], and the net lateral migration in the y direction is approximately zero. The measurements are consistent with findings from earlier numerical and theoretical studies [42,46].

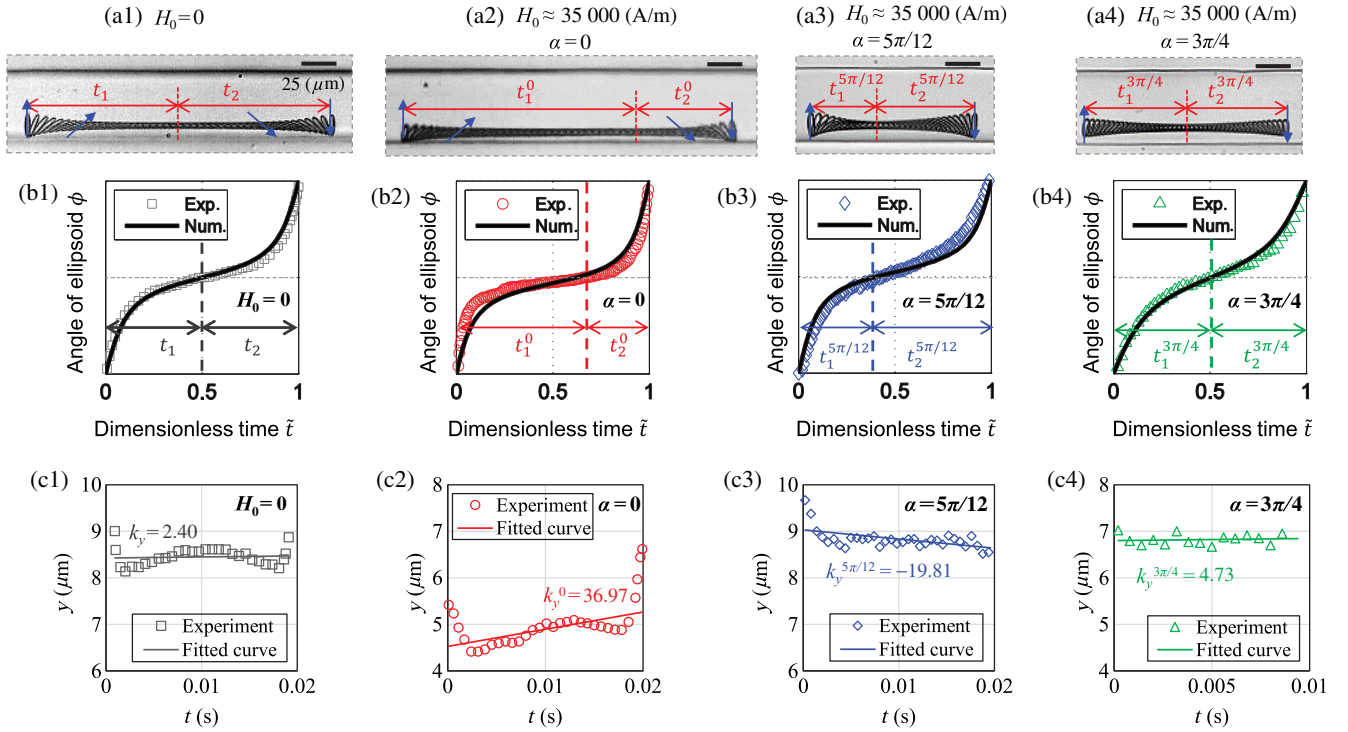


FIG. 5. The rotational and translational dynamics of ellipsoidal particles. (a1)–(a4) Superimposed images for $H_0 = 0$ and $H_0 \approx 35\,000$ A/m with magnetic-field orientation $\alpha = 0$, $\alpha = 5\pi/12$, and $\alpha = 3\pi/4$, respectively. (b1)–(b4) The experimental and numerical angles of ellipsoidal orientation $\phi(\tilde{t})$ within a π period. The symbols represent experimental measurements, and the solid lines represent the numerical solution according to Eq. (7). (c1)–(c4) The experimental measurements of the y position of a particle centroid (y_c) over one rotational period, and their linear fitted curves corresponding to the particles in (a1)–(a4). The slopes k of the linear fitted curve represent the lateral velocities.

With a magnetic field applied, the characteristics of the particle rotation become different, as shown in Figs. 5(b2)–5(b4). The evolution of angle ϕ as a function of time now depends on the direction of the applied magnetic field. Here, we focus on the symmetry or asymmetry of the particle rotation. When $\alpha = 0$, the particle spends a longer time from $\phi = 0$ to $\phi = \pi/2$, i.e., $t_1^0 > t_2^0$ ($\tau > 0.5$), as shown in Fig. 5(b2). The oscillatory motion of the particle seems to closely correlate with the particle rotation [Fig. 5(c2)]. The particle migrates toward the channel center for a longer duration compared to that of the case $H_0 = 0$. The broken asymmetry of the rotation leads to a net lateral migration. When $\alpha = 5\pi/12$, the time spent from $\phi = 0$ to $\phi = \pi/2$, and $\phi = \pi/2$ to $\phi = \pi$ has the relation of $t_1^{5\pi/12} < t_2^{5\pi/12}$ (i.e., $\tau < 0.5$) in Fig. 5(b3). As a result, the particle shows a net migration toward the channel wall [Fig. 5(c3)]. For the case of $\alpha = 3\pi/4$, $t_1^{3\pi/4} = t_2^{3\pi/4}$ ($\tau = 0.5$), as shown in Fig. 5(b4). The net lateral migration of the particle is more or less zero over one rotation cycle [Fig. 5(c4)].

In an attempt to estimate the vertical velocities, the experimental data are fitted by linear lines so that the slopes (k_y , k_y^0 , $k_y^{5\pi/12}$, and $k_y^{3\pi/4}$) represent the net vertical velocities over a π period, as shown in Figs. 5(c1)–5(c4). The superscripts denote the direction of the magnetic field. In the absence of a magnetic field [Fig. 5(c1)], k_y is as small as $k_y^{3\pi/4}$ in Fig. 5(c4), and the vertical velocities in these two cases are at least 5 times smaller than in the other two cases. Furthermore, Fig. 5(c2) shows that k_y^0 is positive and much larger than the slopes in other situations, indicating that the particles migrate toward the channel center when $\alpha = 0$. When the orientation of the magnetic field is $\alpha = 5\pi/12$, the negative $k_y^{5\pi/12}$ reveals that the ellipsoid migrates toward the wall of microfluidic channel.

We also compare the experimental τ with the prediction from the simple theory in Sec. III for different values of α and S , as shown in Fig. 6. In determining the value of S in the experiment, we assume that the particles are in the middle

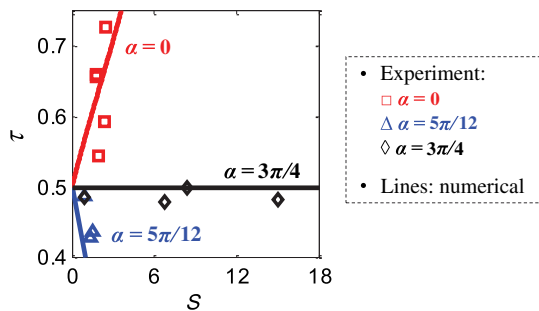


FIG. 6. Comparison of the experimentally measured τ and the theoretical prediction with different S and α values. The symbols are experimental measurements, and the solid lines are calculated according to Eq. (9).

plane of the channel (i.e., $z = 0$), and we evaluate the shear rate based on the undisturbed velocity at the average position of the particle centroid. This evaluation is due to the fact that the particle centroid oscillates in the y direction, and the channel flow thus has a varying shear rate. In addition, we use $r_p = 4$ in the numerical calculations, while, in the experiments, r_p displays some variation. Despite these assumptions and approximations, the experimental data are in good agreement with the theoretical prediction. Figure 6 further demonstrates that the direction of the magnetic field, α , dictates the relation between τ and 0.5, while the relative strength of the magnetic field, S , affects the value of τ . In other words, α and S control the direction and the speed of the lateral migration of the ellipsoidal particles, respectively. While our simple theoretical model is able to predict the migration direction, a three-dimensional numerical approach would be required to account for the particle-fluid and particle-wall hydrodynamic interactions in order to calculate the particle-migration speed.

B. Shape-based separation of microparticles

With a basic understanding of the physical principle of the shape-dependent migration, we apply it to separating the microparticles by shape. According to Fig. 4, there exists a magnetic-field direction α^{\max} that can achieve a maximum τ^{\max} and may cause the fastest migration. However, this angle α^{\max} depends on both r_p and S and is difficult to determine. It is observed that $\alpha = 0$ always leads to $\tau^0 > 0.5$, and that τ^0 is only marginally smaller than τ^{\max} . Thus, we use a perpendicular magnetic field ($H_0 \approx 35000$ A/m, $\alpha = 0$) to investigate the shape-based migration and separation.

We demonstrate the separation of ellipsoids from spheres. The ellipsoidal ($r_p \approx 4.0$) and spherical particles have the same volume but different shapes, as shown in Figs. 7(a1) and 7(a2). In case 1, a mixture of magnetic spherical and ellipsoidal particles ($\chi_p \approx 0.26$) is injected from inlet 2 at a flow rate $Q_2 = 0.2$ $\mu\text{l}/\text{min}$, and the buffer flow of a 40-wt% aqueous-glycerol solution ($\chi_f = 0$) is injected from inlet 1 at a flow rate $Q_1 = 1.0$ $\mu\text{l}/\text{min}$, as shown in Fig. 2(a). At the end of the channel, the ellipsoidal particles migrate toward the centerline, while spherical particles remain at similar initial positions. The corresponding probability density functions (PDFs) of particle distribution in Figs. 7(b1) and 7(b2) reveal a clear separation of different-shaped particles.

The shape-dependent migration applies to both magnetic and nonmagnetic microparticles. This is because magnetic torques will arise as long as the ellipsoidal particle and the fluid have different magnetic susceptibilities according to Eq. (2), and similar asymmetrical particle rotations (see Appendix C) and net lift forces and migration will result. In case 2, we demonstrate the lateral migration of nonmagnetic ellipsoidal particles ($\chi_p = 0$) in an aqueous ferrofluid (EMG 408 Ferrotec,

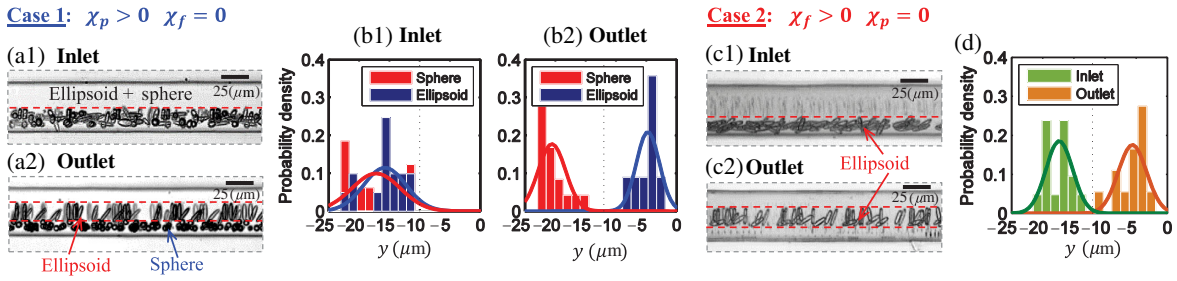


FIG. 7. Separation of ellipsoidal particles from a mixture. (a1),(a2) Superimposed images of the magnetic spheric and ellipsoidal particles at the inlet and the outlet of the microfluidic channel, respectively; (b1),(b2) PDFs of the particle distributions. (c1),(c2) Superimposed images of the nonmagnetic ellipsoidal particles suspended in a ferrofluid at the inlet and the outlet, respectively. (d) PDFs of the particle distributions corresponding to (c1) and (c2). The magnetic intensity of the uniform magnetic field is $H_0 \approx 35000$ A/m and $\alpha = 0$. The width of the microfluidic channel is $w_c = 50 \mu\text{m}$.

diluted with water at 1 : 1; initial susceptibility, $\chi_f = 0.25$). Comparing the particle distributions at the inlet and the outlet in Figs. 7(c1), 7(c2), and 7(d), we observe that the ellipsoidal particles migrate toward the center of the microfluidic channel, similar to magnetic particles suspended in a nonmagnetic fluid.

V. CONCLUSION

In this paper, we present a simple, effective, and tunable technique to control the lateral migration of ellipsoidal microparticles by combining microhydrodynamic flows with a uniform magnetic field. The technique uses magnetically induced torques to alter the symmetry of the particle rotation—and thereby the lateral migration. Theoretical analysis shows that the direction and the strength of the magnetic fields directly affects the degree of rotational asymmetry. Specifically, the direction of the magnetic field determines whether it takes a longer or shorter time when the particles rotate in the first half period of the rotation. The relative strength of the magnetic field to the flow determines the extent of such rotational asymmetry. The particle rotation, in turn, influences the net lift force and the lateral migration velocity. We demonstrate the shape-based separation of microparticles by using the presented mechanism. The shape-dependent migration applies to both magnetic and nonmagnetic particles as long as the particle and the suspending fluid have different magnetic susceptibilities. The proposed technique thus provides a general

mechanism for the separation of microparticles—e.g., various bioparticles—by shape, and it has great potential for various biological and biomedical applications.

ACKNOWLEDGMENTS

The authors gratefully acknowledge the financial support from the Department of Mechanical and Aerospace Engineering, Center for Biomedical Science and Engineering (CBSE) at Missouri University of Science and Technology, and from the Chancellor's Distinguished Fellowship (C. A. S.).

APPENDIX A: STABILITY OF STEADY-STATE ANGLES

Defining a dimensionless total angular velocity $\Omega_c = \omega_c / \dot{\gamma}$, we have $(d\omega_c / d\phi) = \dot{\gamma}(d\Omega_c / d\phi)$, with

$$\frac{d\Omega_c}{d\phi} = \frac{-\sin(2\phi)(r_p^2 - 1) - 2S \cos(2\phi - 2\alpha)}{(r_p^2 + 1)}. \quad (\text{A1})$$

Substituting ϕ_{\pm}^s , we numerically analyze whether their values are negative or positive. A sample evaluation is shown in Fig. (8), where we set $r_p = 4$, $\alpha \in [0, \pi]$, and $S \in [0, 20]$. For $S > S_{\text{cr}}$, it is observed that $[d\omega_c / d\phi]_{\phi_{+}^s}$ is always negative; thus, ϕ_{+}^s is the stable steady angle. The other solution, ϕ_{-}^s , is unstable due to $[d\omega_c / d\phi]_{\phi_{-}^s} > 0$.

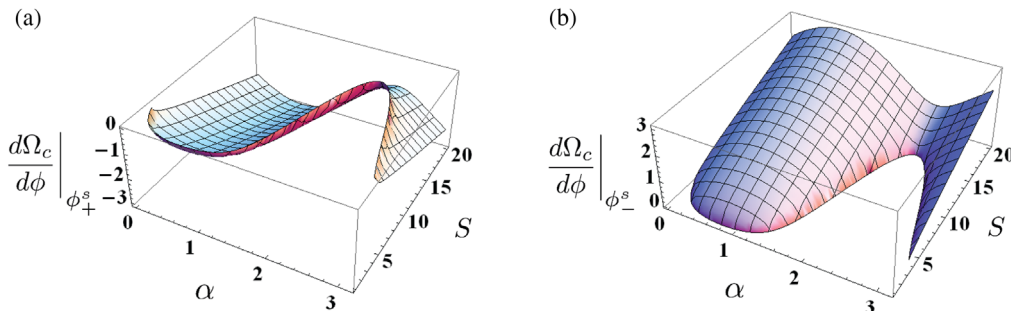


FIG. 8. Three-dimensional graphs of $[d\omega_c / d\phi]_{\phi^s}$ (a) for ϕ_{+}^s and (b) for ϕ_{-}^s . A particle aspect ratio of $r_p = 4$ is used in the numerical evaluation.

TABLE I. Definition of lift, drag, and torque coefficients.

	C_D	C_L	C_T
(i)	$C_{D1} = (F_{x1}/3\pi\eta u_f d_p)$	$C_{L1} = (F_{y1}/3\pi\eta u_f d_p)$	$C_{T1} = (T_{z1}/2\pi\eta u_f d_p^2)$
(ii)	$C_{D2} = (F_{x2}/3\pi\eta\omega_p d_p^2)$	$C_{L2} = (F_{y2}/3\pi\eta\omega_p d_p^2)$	$C_{T2} = (T_{z2}/2\pi\eta\omega_p d_p^2)$
(iii)	$C_{D3} = (F_{x3}/3\pi\eta u_p d_p)$	$C_{L3} = (F_{y3}/3\pi\eta u_p d_p)$	$C_{T3} = (T_{z3}/2\pi\eta u_p d_p^2)$
(iv)	$C_{D4} = (F_{x4}/3\pi\eta v_p d_p)$	$C_{L4} = (F_{y4}/3\pi\eta v_p d_p)$	$C_{T4} = (T_{z4}/2\pi\eta v_p d_p^2)$

APPENDIX B: NUMERICAL ANALYSIS OF A PARTICLE'S LATERAL VELOCITY

The particle transport in a confined microchannel is inherently complex due to the finite size of the particle and its nonspherical shape. Here, we use numerical calculations to understand the effect of parameter τ (or α) on the net lateral migration over one period of rotation. To be consistent with our theoretical analysis, we consider an ellipsoidal particle transported in a simple shear flow bounded by a single wall.

Assuming negligible particle inertia and low-Reynolds-number flows, we decompose the dynamic problem of particle transport into four steady-state problems: (i) $u_f \neq 0$, $\omega_p = 0$, $u_p = 0$, $v_p = 0$; (ii) $u_f = 0$, $\omega_p \neq 0$, $u_p = 0$, $v_p = 0$; (iii) $u_f = 0$, $\omega_p = 0$, $u_p \neq 0$, $v_p = 0$; and (iv) $u_f = 0$, $\omega_p = 0$, $u_p = 0$, $v_p \neq 0$, as shown in Fig. 9. Similar approaches have been used previously to study lift forces on nonspherical particles in simple shear flows [42] and spherical microparticles in rectangular microchannels [20]. For each subproblem, the particle will experience lift (F_y) and drag (F_x) forces and torque (T_z), and we define lift C_L , drag C_D , and torque C_T coefficients as shown in Table I. The coefficients C_L , C_D , and C_T are calculated with the finite-element-method software package COMSOL

MULTIPHYSICS by fixing the particle centroid at (x_0, y_0, z_0) while varying the particle orientation ϕ from 0 to π .

Because of the small particle Reynolds number, the particle motion can be approximated as quasisteady; therefore, the total force and torque are zero. From Eqs. (2), (4), and (5), the magnetic torque can be expressed as $T_{mz} = -\frac{16}{3} \{S\pi ab^2 \eta \dot{\gamma} / [2r_p^2(1-A) + A]\} \sin(2\phi - 2\alpha)$. In the simulations, we use $y_0 = 10 \mu\text{m}$, $a = 8.82 \mu\text{m}$, $b = c = 2.21 \mu\text{m}$, and a simple shear flow $u_f = \dot{\gamma}y$, with $\dot{\gamma} = 500 \text{ 1/s}$. We use a constant $S = 1$ and three different α values (0 , $5\pi/12$, and $3\pi/4$). The corresponding values of τ are 0.58, 0.41, and 0.5, respectively. With the prescribed flow velocity u_f and magnetic torque T_{mz} , we can determine ω_p , u_p , and v_p such that $\sum_{i=1}^4 F_{xi} = 0$, $\sum_{i=1}^4 F_{yi} = 0$, and $\sum_{i=1}^4 T_{zi} + T_{mz} = 0$. We also study the case of $S = 0$, which corresponds to zero magnetic field and $\tau = 0.5$. Figure 9 shows the lateral velocity v_p over one rotational period, and the net shaded area ($\int_0^{T_c} v_p dt$) thus represents the net migration of the particle. As shown in Fig. 9, the net migration direction is in good agreement with our hypothesis: (i) $\int_0^{T_c} v_p dt > 0$, i.e., a net lateral migration toward the channel center when $\tau > 0.5$, in Fig. 9(b); (ii) $\int_0^{T_c} v_p dt < 0$, i.e., toward the channel wall

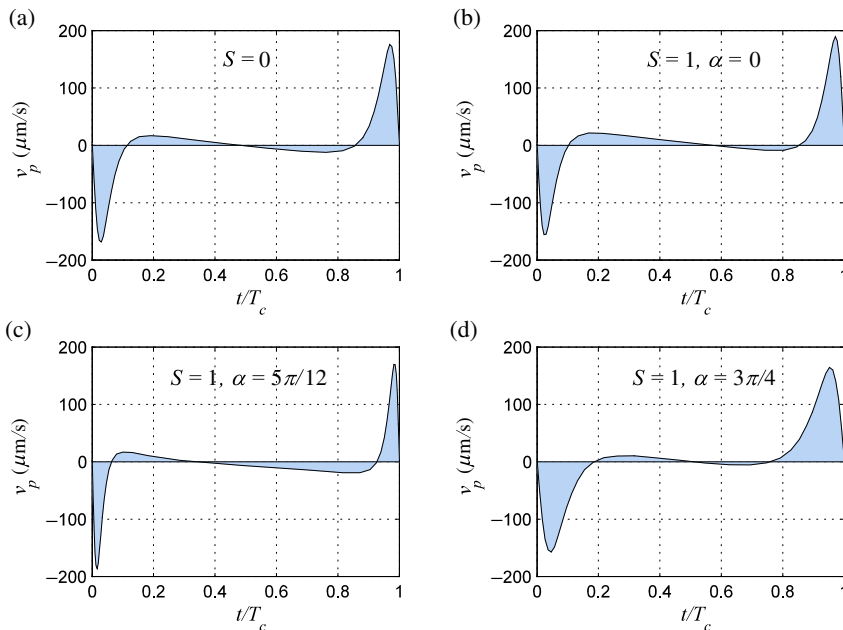


FIG. 9. Lateral migration velocity over one rotational period. (a) $S = 0$. (b) $S = 1$, $\alpha = 0$. (c) $S = 1$, $\alpha = 5\pi/12$. (d) $S = 1$, $\alpha = 3\pi/4$.

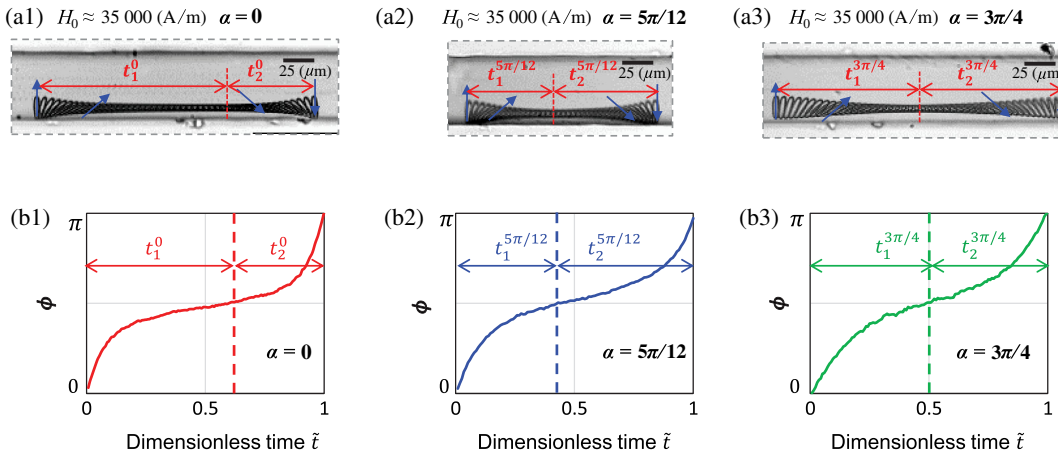


FIG. 10. The rotational dynamics of nonmagnetic particles flowing in a diluted ferrofluid ($\chi_f \approx 0.25$). (a1)–(a3) Superimposed images for $H_0 \approx 35000$ A/m with magnetic-field orientations $\alpha = 0$, $\alpha = 5\pi/12$, and $\alpha = 3\pi/4$, respectively. (b1)–(b3) Experimental angles of the ellipsoidal orientation $\phi(\tilde{t})$ within a π period.

when $\tau < 0.5$, in Fig. 9(c); and (iii) $\int_0^T v_p dt \approx 0$, i.e., a negligible lateral migration when $\tau = 0.5$, in Figs. 9(a) and 9(d). Although our numerical model is a simplified representation of the complex particle dynamics in confined microchannels, it qualitatively explains the effect on the magnetic field and τ on the direction of the lateral migration, as observed in the experiments.

APPENDIX C: ROTATIONAL DYNAMICS OF NONMAGNETIC PARTICLES IN A FERROFLUID

Additionally, we experimentally measure particle rotational dynamics of a nonmagnetic particle ($\chi_p = 0$) in a 50% diluted ferrofluid (EMG 408, Ferrotec), which has an initial magnetic susceptibility $\chi_f \approx 0.25$. The total flow rate is $Q_t = 1.2 \mu\text{l}/\text{min}$, and the applied magnetic field is $H_0 \approx 35000$ A/m. As can be seen in Fig. 10, the magnetic field influences the rotational dynamics of nonmagnetic particle in a manner identical to paramagnetic particles. The asymmetric particle rotation thus results in a similar shape-dependent migration for any particle and fluid pair that has differing magnetic susceptibilities.

[1] K. D. Young, The selective value of bacterial shape, *Microbiol. Mol. Biol. Rev.* **70**, 660 (2006).
 [2] Harriet Gershon and David Gershon, The budding yeast, *Saccharomyces cerevisiae*, as a model for aging research: A critical review, *Mech. Ageing Dev.* **120**, 1 (2000).
 [3] I. Herskowitz, Life cycle of the budding yeast *Saccharomyces cerevisiae*, *Microbiol. Rev.* **52**, 536 (1988).
 [4] Nicholas M. Anstey, Bruce Russell, Tsin W. Yeo, and Ric N. Price, The pathophysiology of vivax malaria, *Trends Parasitol.* **25**, 220 (2009).
 [5] P. S. Frenette, Sickle cell vaso-occlusion: Multistep and multicellular paradigm, *Curr. Opin. Hematol.* **9**, 101 (2002).
 [6] Robert Van Reis and Andrew Zydny, Membrane separations in biotechnology, *Curr. Opin. Biotechnol.* **12**, 208 (2001).

[7] Ali Asgar S. Bhagat, Hansen Bow, Han Wei Hou, Swee Jin Tan, Jongyoon Han, and Chwee Teck Lim, Microfluidics for cell separation, *Med. Biol. Eng. Comput.* **48**, 999 (2010).
 [8] A. Karimi, S. Yazdi, and A. M. Ardekani, Hydrodynamic mechanisms of cell and particle trapping in microfluidics, *Biomicrofluidics* **7**, 021501 (2013).
 [9] C. Wyatt Shields, Catherine D. Reyes, and Gabriel P. López, Microfluidic cell sorting: A review of the advances in the separation of cells from debulking to rare cell isolation, *Lab Chip* **15**, 1230 (2015).
 [10] Sari Sugaya, Masumi Yamada, and Minoru Seki, Observation of nonspherical particle behaviors for continuous shape-based separation using hydrodynamic filtration, *Biomicrofluidics* **5**, 024103 (2011).
 [11] Jason P. Beech, Stefan H. Holm, Karl Adolfsson, and Jonas O. Tegenfeldt, Sorting cells by size, shape and deformability, *Lab Chip* **12**, 1048 (2012).
 [12] Kerwin Kwek Zeming, Shashi Ranjan, and Yong Zhang, Rotational separation of non-spherical bioparticles using I-shaped pillar arrays in a microfluidic device, *Nat. Commun.* **4**, 1625 (2013).
 [13] Soojung Claire Hur, Sung-Eun Choi, Sunghoon Kwon, and Dino Di Carlo, Inertial focusing of non-spherical microparticles, *Appl. Phys. Lett.* **99**, 044101 (2011).
 [14] Mahdokht Masaeli, Elodie Sollier, Hamed Amini, Wenbin Mao, Kathryn Camacho, Nishit Doshi, Samir Mitragotri, Alexander Alexeev, and Dino Di Carlo, Continuous Inertial Focusing and Separation of Particles by Shape, *Phys. Rev. X* **2**, 031017 (2012).
 [15] Ana Valero, Thomas Braschler, Alex Rauch, Nicolas Demierre, Yves Barral, and Philippe Renaud, Tracking and synchronization of the yeast cell cycle using dielectrophoretic opacity, *Lab Chip* **11**, 1754 (2011).
 [16] John Dubose, Xinyu Lu, Saurin Patel, Shizhi Qian, Sang Woo Joo, and Xiangchun Xuan, Microfluidic electrical sorting of particles based on shape in a spiral microchannel, *Biomicrofluidics* **8**, 014101 (2014).
 [17] Xinyu Lu and Xiangchun Xuan, Elasto-inertial pinched flow fractionation for continuous shape-based particle separation, *Anal. Chem.* **87**, 11523 (2015).
 [18] Xinyu Lu, Lin Zhu, Ri-mao Hua, and Xiangchun Xuan, Continuous sheath-free separation of particles by shape in viscoelastic fluids, *Appl. Phys. Lett.* **107**, 264102 (2015).

- [19] Yilong Zhou and Xiangchun Xuan, Diamagnetic particle separation by shape in ferrofluids, *Appl. Phys. Lett.* **109**, 102405 (2016).
- [20] Dino Di Carlo, Jon F. Edd, Katherine J. Humphry, Howard A. Stone, and Mehmet Toner, Particle Segregation and Dynamics in Confined Flows, *Phys. Rev. Lett.* **102**, 094503 (2009).
- [21] X. Grandchamp, G. Coupier, A. Srivastav, C. Minetti, and T. Podgorski, Lift and Down-Gradient Shear-Induced Diffusion in Red Blood Cell Suspensions, *Phys. Rev. Lett.* **110**, 108101 (2013).
- [22] J. Dupire, M. Socol, and A. Viallat, Full dynamics of a red blood cell in shear flow, *Proc. Natl. Acad. Sci. U.S.A.* **109**, 20808 (2012).
- [23] Z. Y. Luo and B. F. Bai, Dynamics of nonspherical compound capsules in simple shear flow, *Phys. Fluids* **28**, 101901 (2016).
- [24] J. M. Skotheim and T. W. Secomb, Red Blood Cells and Other Nonspherical Capsules in Shear Flow: Oscillatory Dynamics and the Tank-Treading-to-Tumbling Transition, *Phys. Rev. Lett.* **98**, 078301 (2007).
- [25] P. M. Vlahovska, T. Podgorski, and C. Misbah, Vesicles and red blood cells in flow: From individual dynamics to rheology, *C.R. Phys.* **10**, 775 (2009).
- [26] Nicole Pamme and Claire Wilhelm, Continuous sorting of magnetic cells via on-chip free-flow magnetophoresis, *Lab Chip* **6**, 974 (2006).
- [27] Nicole Pamme, Continuous flow separations in microfluidic devices, *Lab Chip* **7**, 1644 (2007).
- [28] Sally A. Peyman, Er Yee Kwan, Oliver Margaron, Alexander Iles, and Nicole Pamme, Diamagnetic repulsion—A versatile tool for label-free particle handling in microfluidic devices, *J. Chromatogr. A* **1216**, 9055 (2009).
- [29] Julius Adams Stratton, *Electromagnetic Theory* (Adams Press, Chicago, 2007).
- [30] Melissa D. Krebs, Randall M. Erb, Benjamin B. Yellen, Bappaditya Samanta, Avinash Bajaj, Vincent M. Rotello, and Eben Alsberg, Formation of ordered cellular structures in suspension via label-free negative magnetophoresis, *Nano Lett.* **9**, 1812 (2009).
- [31] Ayse R. Kose, Birgit Fischer, Leidong Mao, and Hur Koser, Label-free cellular manipulation and sorting via biocompatible ferrofluids, *Proc. Natl. Acad. Sci. U.S.A.* **106**, 21478 (2009).
- [32] Wujun Zhao, Rui Cheng, Joshua R. Miller, and Leidong Mao, Label-free microfluidic manipulation of particles and cells in magnetic liquids, *Adv. Funct. Mater.* **26**, 3916 (2016).
- [33] Eun Hee Kim, Hyo Sook Lee, Byung Kook Kwak, and Byung Kee Kim, Synthesis of ferrofluid with magnetic nanoparticles by sonochemical method for MRI contrast agent, *J. Magn. Magn. Mater.* **289**, 328 (2005).
- [34] I Torres-Díaz and C Rinaldi, Recent progress in ferrofluids research: Novel applications of magnetically controllable and tunable fluids, *Soft Matter* **10**, 8584 (2014).
- [35] H. Raich and P. Blumler, Design and construction of a dipolar halbach array with a homogeneous field from identical bar magnets: NMR Mandhalas, *Concepts Magn. Reson., Part B* **23B**, 16 (2004).
- [36] Ran Zhou and Cheng Wang, Acoustic bubble enhanced pinched flow fractionation for microparticle separation, *J. Micromech. Microeng.* **25**, 084005 (2015).
- [37] C. C. Ho, A. Keller, J. A. Odell, and R. H. Ottewill, Preparation of monodisperse ellipsoidal polystyrene particles, *Colloid Polym. Sci.* **271**, 469 (1993).
- [38] Roel Wirix-Speetjens, Wim Fyen, Jo De Boeck, and Gustaaf Borghs, Single magnetic particle detection: Experimental verification of simulated behavior, *J. Appl. Phys.* **99**, 103903 (2006).
- [39] B. P. Ho and L. G. Leal, Inertial migration of rigid spheres in two-dimensional unidirectional flows, *J. Fluid Mech.* **65**, 365 (1974).
- [40] M. D. Abramoff, P. J. Magalhes, and S. J. Ram, Image processing with IMAGEJ, *Biophotonics Int.* **11**, 36 (2004).
- [41] F. P. Bretherton, The motion of rigid particles in a shear flow at low Reynolds number, *J. Fluid Mech.* **14**, 284 (1962).
- [42] E. Gavze and M. Shapiro, Particles in a shear flow near a solid wall: Effect of nonsphericity on forces and velocities, *Int. J. Multiphase Flow* **23**, 155 (1997).
- [43] Kelli B. Moses, Suresh G. Advani, and Andreas Reinhardt, Investigation of fiber motion near solid boundaries in simple shear flow, *Rheol. Acta* **40**, 296 (2001).
- [44] G. B. Jeffery, The motion of ellipsoidal particles immersed in a viscous fluid, *Proc. R. Soc. A* **102**, 161 (1922).
- [45] L. G. Leal, Particle motions in a viscous fluid, *Annu. Rev. Fluid Mech.* **12**, 435 (1980).
- [46] Seung-Man Yang and Gary L. Leal, Particle motion in Stokes flow near a plane fluid-fluid interface. Part 2. Linear shear and axisymmetric straining flows, *J. Fluid Mech.* **149**, 275 (1984).
- [47] J. Happel and H. Brenner, *Low Reynolds Number Hydrodynamics* (Prentice-Hall, Englewood Cliffs, NJ, 1983).
- [48] Nipa A. Mody and Michael R. King, Three-dimensional simulations of a platelet-shaped spheroid near a wall in shear flow, *Phys. Fluids* **17**, 113302 (2005).
- [49] C. Jayageeth, Vivek Inder Sharma, and Anugrah Singh, Dynamics of short fiber suspensions in bounded shear flow, *Int. J. Multiphase Flow* **35**, 261 (2009).
- [50] I. Torres-Díaz and C. Rinaldi, Brownian dynamics simulations of ellipsoidal magnetizable particle suspensions, *J. Phys. D* **47**, 235003 (2014).
- [51] A. Okagawa, R. G. Cox, and S. G. Mason, Particle behavior in shear and electric fields. VI. The microrheology of rigid spheroids, *J. Colloid Interface Sci.* **47**, 536 (1974).
- [52] A. D. Shine and R. C. Armstrong, The rotation of a suspended axisymmetric ellipsoid in a magnetic field, *Rheol. Acta* **26**, 152 (1987).
- [53] R. S. Allan and S. G. Mason, Particle behaviour in shear and electric fields. II. Rigid rods and spherical doublets, *Proc. R. Soc. A* **267**, 62 (1962).